

# RadProPoser: A Framework for Human Pose Estimation with Uncertainty Quantification from Raw Radar Data

Jonas Leo Mueller<sup>1</sup>, Lukas Engel<sup>1</sup>, *Graduate Student Member, IEEE*, Eva Dorschky<sup>1</sup>, *Member, IEEE*, Daniel Krauss<sup>1</sup>, *Graduate Student Member, IEEE*, Ingrid Ullmann<sup>1</sup>, *Member, IEEE*, Martin Vossiek<sup>1</sup>, *Fellow, IEEE*, Bjoern M. Eskofier<sup>1</sup>, *Senior Member, IEEE*

**Abstract**—Radar-based human pose estimation (HPE) provides a privacy-preserving, illumination-invariant sensing modality but is challenged by noisy, multipath-affected measurements. We introduce RadProPoser, a probabilistic encoder–decoder architecture that processes complex-valued radar tensors from a compact 3-transmitter, 4-receiver MIMO radar. By incorporating variational inference into keypoint regression, RadProPoser jointly predicts 26 three-dimensional joint locations alongside heteroscedastic aleatoric uncertainties and can be recalibrated to predict total uncertainty. We explore different probabilistic formulations using both Gaussian and Laplace distributions for the latent priors and likelihoods. On our newly released dataset with optical motion-capture ground truth, RadProPoser achieves an overall mean per-joint position error (MPJPE) of 6.425 cm, with 5.678 cm at the 45° aspect angle. The learned uncertainties exhibit strong alignment with actual pose errors and can be calibrated to produce reliable prediction intervals, with our best configuration achieving an expected calibration error of 0.021. As an additional demonstration, sampling from these latent distributions enables effective data augmentation for downstream activity classification, resulting in an F1 score of 0.870. To our knowledge, this is the first end-to-end radar tensor–based HPE system to explicitly model and quantify per-joint uncertainty from raw radar tensor data in an end-to-end fashion, establishing a foundation for explainable and reliable human motion analysis in radar applications.

**Index Terms**—Radar-based Human Pose Estimation, Deep Learning, Probabilistic Modeling, Uncertainty Estimation, Optical Motion Capture

## I. INTRODUCTION

Machine learning models, as a core component of artificial intelligence (AI) systems, are increasingly deployed in high-risk domains, raising critical concerns about transparency, reliability, and interpretability. In safety-critical areas such as medical diagnostics [1], [2] and autonomous systems [3], [4], uncertainty-aware machine learning has become a foundational requirement for reliable decision-making under conditions of limited or noisy observations [5]. The European Union’s AI Act [6] highlights the need for high-risk AI systems to be

sufficiently transparent so that their outputs can be interpreted and acted upon appropriately. Calibrated uncertainty estimates can contribute to this transparency by clarifying the model’s reliability and its confidence in predictions, particularly when sensor data are incomplete, ambiguous, or noisy.

These demands are especially pressing in sensor-based systems that rely on non-traditional modalities, including radar [7], [8], [9], [10], [11], [12], LiDAR [13], and ultrasound [14]. Unlike high-resolution, structured data from RGB cameras [15], these sensing modalities produce sparse or indirect measurements that require inference-driven reconstruction and are highly susceptible to noise and environmental artifacts in the deep learning context. Radar, in particular, is affected by thermal, quantization, and phase noise [16], along with environment-dependent effects such as multipath propagation, refraction, and scattering [17]. These characteristics increase the risk of overconfident predictions from point-estimate models, making the ability to express data-dependent uncertainty essential for trustworthy downstream use.

Radar-based human pose estimation (HPE) exemplifies these challenges while offering unique advantages, such as non-contact sensing, robustness to lighting, material penetration capabilities, and enhanced privacy [11], [7]. Beyond pose estimation, radar has found applications in vital signs monitoring [1], [2], gait analysis [18], and activity recognition [19]. Radar HPE methods typically fall into two categories, those using compressed point clouds, often derived using Constant False Alarm Rate (CFAR) algorithms with hand-tuned parameters [20], [21], and radar tensor approaches (RTA) that operate on the minimally processed radar cube [11], [7], [22]. While RTA methods may generally outperform point cloud approaches in accuracy [11], they also demand greater computational resources and memory, especially with large antenna configurations. Moreover, many existing RTA pipelines rely on RGB-based systems for 3D ground truth generation, which may introduce ambiguity from depth estimation [23] and susceptibility to occlusions [24]. For instance, Lee et al. [7] used two orthogonally mounted radar sensors [25] for 2D keypoint detection in image space, followed by a lifting network to estimate 3D poses, achieving a mean per-joint position error (MPJPE) of 6.82 cm under simple actions without inter-subject evaluation. Zhu et al. [12] improved 2D detection performance by using probabilistic point cloud-guided features as anchors for radar tensor processing. More recently, Ho et al. [11] introduced a larger-scale dataset with a 12×16 antenna array, multi-modal ground-truth generation from RGB and LiDAR [26], and single frame full radar cube

This work has been submitted to the IEEE for possible publication. Copyright may be transferred without notice, after which this version may no longer be accessible.

This work was (partly) funded by the Deutsche Forschungsgemeinschaft (DFG, German Research Foundation) – SFB 1483 – Project-ID 442419336, EmpkinS. Jonas Mueller, Eva Dorschky, Daniel Krauss and Bjoern M. Eskofier are with the Machine Learning and Data Analytics Lab, Friedrich-Alexander-Universität Erlangen-Nürnberg, Germany (e-mail: jonas.leo.mueller@fau.de, eva.dorschky@fau.de, daniel.k.krauss@fau.de)

Lukas Engel, Ingrid Ullmann and Martin Vossiek are with the Institute of Microwaves and Photonics, Friedrich-Alexander-Universität Erlangen-Nürnberg, Germany (e-mail: lukas.le.engel@fau.de, ingrid.ullmann@fau.de, martin.vossiek@fau.de)

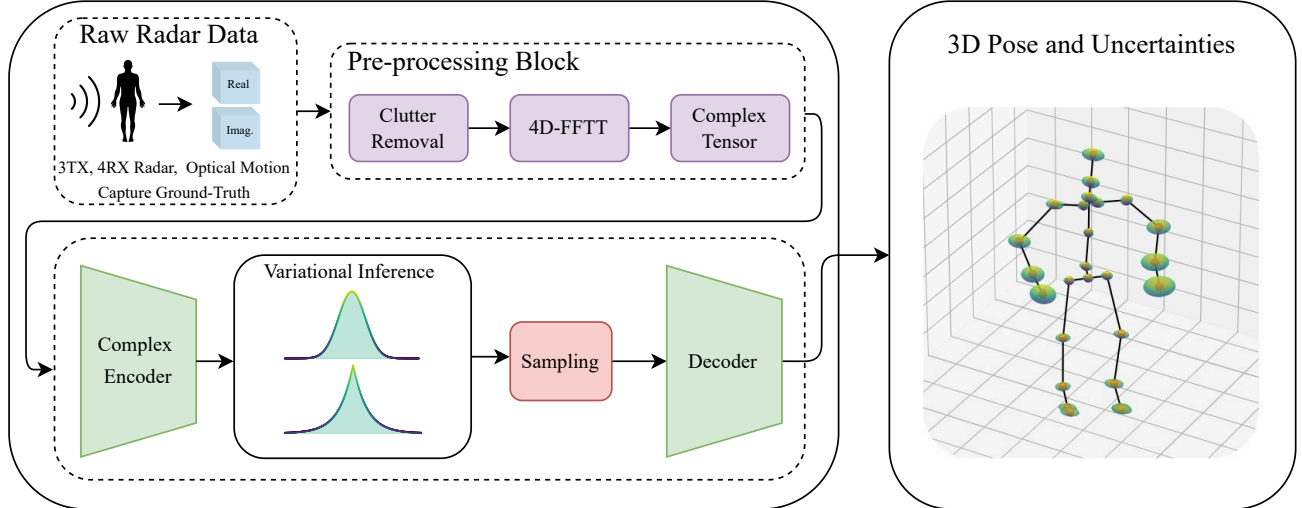


Fig. 1. Overview of our approach. The raw radar data is encoded into a distribution over latent codes and then used for probabilistic pose estimation and uncertainty quantification. We use Gaussian and Laplace Priors in the latent space. On the right, uncertainties are presented as hulls defined by the standard deviations in the x, y, and z direction.

processing, reaching an MPJPE of 9.91 cm across diverse scenarios. These advances highlight the trade-offs between antenna array size, computational requirements, and performance that remain important considerations for practical deployment.

While most radar-based HPE efforts have focused on improving keypoint accuracy, the explicit modeling of aleatoric predictive uncertainty remains limited. Some approaches have addressed uncertainty indirectly, for example, through loss reweighting strategies [27] or modeling total uncertainty with generative models with radar point clouds [28], [29], thereby reporting point predictions. Broader applications of uncertainty estimation have also emerged in areas like radar-based human tracking [30], LiDAR-based 3D object detection [31], or radar SLAM [32]. However, within radar tensor-based HPE specifically, no prior work directly incorporates data-dependent aleatoric uncertainty modeling into the pose estimation pipeline.

In parallel, research in other modalities, particularly vision-based HPE, has progressed along two main directions in uncertainty modeling. These are uncertainty-aware methods and uncertainty quantification methods. The first category focuses on using uncertainty during training to improve supervision or loss design, often without explicitly reporting uncertainty estimates at inference time. The second category aims to explicitly model and quantify predictive uncertainties, including aleatoric and epistemic components. Uncertainty-aware methods include approaches that incorporate uncertainties as supervisory signals, such as annotation variance [33] or prediction uncertainty for training data sampling [34], as well as generative techniques such as denoising diffusion models [35], [36], [37], where probabilistic predictions are sampled multiple times and averaged. In contrast, uncertainty quantification methods aim to estimate the uncertainty associated with model predictions directly. Normalizing Flows [38], [39] have been used to estimate 3D shape and poses with uncertainty quantification,

where the Pearson correlation between learned uncertainties and prediction errors provides a quantitative measure of uncertainty quality. Similarly, Prokudin et al. [40] regress angular von Mises distributions over object poses to capture total predictive uncertainty. Bramlage et al. [41] adopt an evidential regression framework that places priors over a  $t$ -distribution to jointly model aleatoric and epistemic uncertainty in pose estimation. Most notably, [42], [43] show how aleatoric uncertainties can be regressed directly for computer vision and pose estimation applications by assuming gaussian distributions. While these approaches demonstrate substantial progress in vision-based settings, the factorization of uncertainty, particularly the quantification of aleatoric uncertainty from RTAs in radar-based HPE, remains underexplored. To address this gap, we propose RadProPoser (RPP), a probabilistic model that operates directly on complex-valued radar tensors acquired from a sparse MIMO radar system with three transmit and four receive antennas (see Figure 1).

Our approach builds upon the backbone architecture introduced by Ho et al. [11] for processing raw radar tensors, and extends it by incorporating temporal modeling to capture motion dynamics more effectively. Additionally, we integrate a variational inference framework into the architecture, enabling principled uncertainty quantification. This integration is motivated by the growing use of variational methods in radar applications motivated by their robustness to noisy representations, including representation learning [44], MIMO detection [45], user localization [46], indoor drone sensing [47], or fall detection [48]. Our approach explores alternative latent space distributions, including parametric priors (Gaussian, Laplace) and more flexible representations like Normalizing Flows, enabling the model to learn data-dependent aleatoric uncertainty through latent distribution sampling. We then apply systematic recalibration of the predictive distributions to additionally estimate total uncertainty, encompassing both aleatoric and

epistemic components, following the method established by [49]. Unlike previous approaches that rely on RGB-based ground truth, we introduce a new dataset with accurate optical motion capture (OMC) ground-truth and provide open access to our training code<sup>1</sup> and dataset<sup>2</sup>. We further demonstrate the utility of a sparse antenna configuration, improving scalability for field applications such as biomechanics (see Table I). Finally, we analyze the structure of the learned latent space and demonstrate its potential for downstream generative tasks such as activity classification.

The structure of this paper is as follows: Section II provides an overview of the relevant literature. Section III details the experimental setup, the derivation of our RadProPoser model, and the loss formulation. Our experiments, results, discussion, and limitations are presented in Sections IV, V, VI, and VII, respectively. Finally, Section VIII summarizes our findings and outlines directions for future research.

## II. THEORETICAL BACKGROUND

### A. Data Representations in Radar-based Human Pose Estimation

In radar-based signal processing, transmitted and received signals are mixed to form the beat signal, from which target position and velocity are extracted [50]. These signals are digitized by the analog-to-digital converter (ADC) and represented as complex-valued radar cubes. Fast Fourier Transforms (FFT) are typically applied across the ADC sample, chirp, azimuth, and elevation dimensions to derive range, velocity (via Doppler), and spatial location [51], [52]. Most radar-based HPE approaches build on this representation [8], [9], [7], [11], varying in preprocessing complexity—from raw ADC data preserving real and imaginary components [53], to magnitude-based slicing of the FFT-processed cube [7], to heavily compressed radar point clouds via CFAR [10]. Recent work has also integrated learnable signal processing, such as FFT layers embedded in neural networks [54], [55]. To preserve the full signal content and minimize information loss, we adopt a low-compression approach operating directly on complex-valued radar tensors. Although the FFT is a linear operation, we follow the common convention of referring to FFT-processed data as raw data, and by limiting preprocessing to this step, we ensure that uncertainty in our results can be attributed to the data rather than upstream signal manipulation.

### B. 3D Pose estimation approaches for radar

Human pose estimation in the vision domain is a well-established research area [15], [56], with a wide range of approaches addressing the task under varying conditions. Broadly, existing methods can be categorized into multi-person and single-person pose estimation. In this work, we focus on the single-person setting and therefore limit our discussion to relevant literature within this scope. Single-person pose estimation methods are commonly classified into top-down and bottom-up approaches. Top-down methods first apply a

person detection stage to localize the subject in the image, followed by a dedicated pose estimation module applied to the detected region. In contrast, bottom-up methods directly predict keypoint locations in the image, and subsequently group them into skeletons.

Models can also be categorized as direct or indirect pose estimators. In the former, the 3D pose is estimated directly in a single forward pass, in the latter, the 3D pose is estimated from 2D poses, typically by exploiting the temporal context of 2D pose sequences using lifting models. Smartphone-based models, for example, estimate the 3D pose directly to reduce computational resources [57], [58], while most state-of-the-art approaches achieving the highest accuracies use 2D-to-3D lifting with transformer models to exploit the context within and across frames [59], [60].

In the radar domain Lee et al. [7] use ground-truth values in image space and therefore rely on a 2D keypoint detection model, followed by a lifting model for 3D regression. Ho et al. use 3D ground truth estimated from LiDAR and RGB data, and therefore rely on a direct 3D prediction model. This aligns with most radar-based HPE approaches, which often use compressed radar-cube representations, such as magnitude-based range-Doppler maps [9], [8], where the 3D coordinates of a pose are regressed directly. Pose estimation models in the vision domain can be trained from two main perspectives. The first approach discretizes the input image into a set of bins [61], and uses an appropriate loss function, such as focal loss, to predict logits for each pixel (in 2D) or voxel (in 3D). In some cases, heatmaps are also used by placing Gaussian distributions over the keypoints of interest, which are then regressed from the image inputs [62]. The second approach directly regresses the continuous 3D output [63], which is typically applied when using optical motion capture data as ground truth to avoid quantization noise. Ho et al. [11] adopt a classification-based approach to localize the root joint, followed by a regression head to estimate the offsets for the remaining joints. This two step procedure stems from their ground-truth estimation pipeline, based on RGB pixel data.

In this study, we adopt a direct 3D pose estimation pipeline in an end-to-end fashion, consistent with regression-based approaches. This design choice reduces the influence of pose estimation strategy on the resulting uncertainty estimates, ensuring that they primarily reflect characteristics of the input data itself. To ensure comparability with Ho et al., we similarly estimate the pose from FFT processed raw radar tensor.

### C. Aleatoric Uncertainty Modeling in Deep Learning

Uncertainty in deep learning predictions can be decomposed into two types, epistemic uncertainty  $\sigma_{\text{epistemic}}^2$ , arising from limited model knowledge, and aleatoric uncertainty  $\sigma_{\text{aleatoric}}^2$ , caused by inherent noise in the observations [43]. In this work, we focus on modeling heteroscedastic aleatoric uncertainty, where the observation noise varies with each input. This can be achieved by learning a predictive distribution and minimizing the corresponding negative log-likelihood (NLL). Let  $y$  denote the target vector,  $\mu_{\theta}(x)$  the predicted mean, given a neural network parameterized by  $\theta$ , and  $N$  the data sample size.

<sup>1</sup><https://github.com/jonasmueller/RadProPoserCode.git>

<sup>2</sup><https://doi.org/10.5281/zenodo.14738837>

TABLE I  
RAW TENSOR-BASED RADAR POSE ESTIMATION DATASETS

Authors	Ground truth	Radar Configuration	Evaluation	2D/3D	Keypoints	Method	Reported Score
Ho et al. [11]	RGB, Lidar	12 TX, 16 RX	MPJPE	3D	15	3D-HR-layers	9.91 cm
Lee et al [7]	RGB	2 × 3 TX, 4 RX	MPJPE	2D	14	Multi-stage feature fusion	6.82 cm
Zhu et al. [12]	RGB	2 × 3 TX, 4 RX	OKS	2D	14	Pointcloud-based prob. maps	69.9 AP
Ours	MoCap	3 TX, 4 RX	MPJPE	3D	26	Prob. Modeling	6.425 cm

MPJPE: Mean per-joint position error, RX: Transmitter, TX: Receiver, OKS: Object-keypoint-similarity, AP: Average Precision.

Under a Gaussian likelihood with constant variance  $\sigma^2$ , the NLL becomes

$$\mathcal{L}_{\text{Gauss.}} = \sum_{i=1}^N \frac{1}{2} \log(2\pi\sigma^2) + \frac{1}{2\sigma^2} (y_i - \mu_{\theta}(x_i))^2, \quad (1)$$

which, up to constants, reduces to the mean squared error (MSE) when  $\sigma^2$  is fixed

$$\mathcal{L}_{\text{MSE}} = \frac{1}{N} \|\mathbf{y} - \boldsymbol{\mu}_{\theta}(\mathbf{x})\|_2^2. \quad (2)$$

Likewise, assuming a Laplace likelihood with constant scale  $b$ , the NLL is

$$\mathcal{L}_{\text{Lap.}} = \sum_{i=1}^N \log(2b) + \frac{|y_i - \mu_{\theta}(x_i)|}{b}, \quad (3)$$

which simplifies to the mean absolute error (MAE) for fixed  $b$

$$\mathcal{L}_{\text{MAE}} = \frac{1}{N} \|\mathbf{y} - \boldsymbol{\mu}_{\theta}(\mathbf{x})\|_1. \quad (4)$$

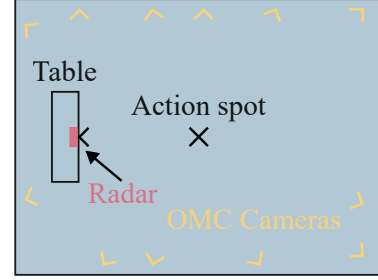
To capture heteroscedastic uncertainty, our model is extended to also predict the per-dimension variance  $\sigma_{\theta}^2(x)$  or scale  $b_{\theta}(x)$  alongside the mean. In the Gaussian case, this yields

$$\mathcal{L}_{\text{Gauss.}} = \frac{1}{2} \sum_{i=1}^N \log(2\pi\sigma_{\theta}^2(x_i)) + \frac{(y_i - \mu_{\theta}(x_i))^2}{\sigma_{\theta}^2(x_i)}, \quad (5)$$

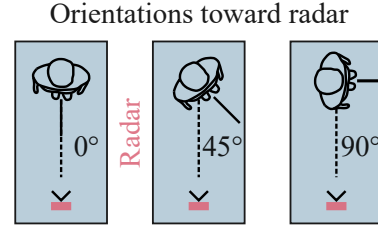
and in the Laplace case,

$$\mathcal{L}_{\text{Lap.}} = \sum_{i=1}^N \log(2b_{\theta}(x_i)) + \frac{|y_i - \mu_{\theta}(x_i)|}{b_{\theta}(x_i)}. \quad (6)$$

Since for HPE our inputs are multi-dimensional we can extend the formalization to additionally model the per dimension variances as well, therefore the per-dimension mean, variance or scale become vectors,  $\boldsymbol{\mu}_{\theta}(\mathbf{x})$ ,  $\boldsymbol{\sigma}_{\theta}^2(\mathbf{x})$ ,  $\mathbf{b}_{\theta}(\mathbf{x})$ . For computational simplicity we can assume independence between dimensions [39], thereby just adding another index to each predicted mean and variance, or in an additional step optimize a multivariate Gaussian with covariance matrix in the likelihood function [42] to account for correlations in the dimensions. We refer to Section III for the derivation of our loss functions for all models. In summary, modeling heteroscedastic aleatoric uncertainty allows deep learning models to express input-dependent noise. By learning the parameters of a predictive distribution and optimizing the corresponding NLL, the model can effectively capture varying levels of uncertainty inherent in the data.



a)



b)

Fig. 2. Overview of a) the recording space and b) the data collection conditions [64].

### III. METHODS

#### A. Dataset

The dataset contains radar recordings time-synchronised with OMC. Figure 2 gives an overview of the recording space and data recording. All information regarding our measurement setup can additionally be found in [64]. We use a frame rate of 15 frames per second for both radar and OMC. We record data from 12 participants (four female, eight male, age  $28.92 \pm 3.15$  years, height  $176.25 \pm 6.25$  cm, weight  $72.33 \pm 12.37$  kg) performing nine actions. The movements consist of left upper limb extension, right upper limb extension, bilateral upper limb extension, bicep curls, front arm rotation, trunk forward bending, left front lunge, right front lunge or squats. The exercises are performed at three angles to the radar,  $0^\circ$ ,  $45^\circ$  and  $90^\circ$ . Each motion sequence is recorded for 36 seconds and repeated three times from the different angle perspectives. The test recording was 3.55 m x 3.05 m in the centre of a room of 10.60 m length, 4.72 m width and 3.27 m height, with the radar facing the test area. To ensure the extraction of a reliable skeleton from the OMC system, each sequence began with a T-pose, followed by the action shortly after the start of the recording. The data used in this study were collected and

TABLE II  
RADAR SYSTEM PARAMETER SETTINGS

Parameter	Value
Frequency	60 GHz
Radio-frequency bandwidth	$\approx 1.02$ GHz
Frame rate	15 Hz
Chirp duration	$\approx 17$ $\mu$ s
Samples per chirp	64
ADC sampling frequency	3.8 MHz
Chirps	128
Number of transmitter antennas	3
Number of receiver antennas	4
TDM-MIMO virtual data channels	12

ADC: analog-to-digital converter, TDM: time-division multiplexing, MIMO: multiple-input multiple-output.

processed in accordance with ethical guidelines and approved by an appropriate ethics review board (Protocol #22-437-B). All participants provided informed consent.

1) *Radar System*: To collect the radar data, we use a Texas Instruments IWR6843AOPEVM radar [65] with four receiver and three transmitter antennas arranged in an L-shaped virtual antenna array. We use time division multiplexing (TDM) where each antenna is activated sequentially. We also use a hardware trigger to synchronise the measurements with the OMC system. The table II summarizes the radar configuration settings. We use padding to improve our resolution after the FFT, as padding the radar cube before performing an FFT increases the number of frequency bins, effectively improving resolution and allowing finer discrimination of target ranges or velocities.

2) *Motion Capture System*: We use an OMC to increase the accuracy of the ground truth data we generate. We use the Optitrack Flex 13 [66] OMC system. Participants are instructed to wear a suit, hat and shoes fitted with infrared markers sensitive to the OMC system. The system uses 12 infrared cameras placed around the room to measure the reflections of the markers, which indicate the position of the human anatomy. We use Optitrack’s Motive:Body software (version 2.3.1) to track these markers.

## B. Pose Estimation Network

The RadProPoser (RPP) architecture (Figure 3) is a function  $\Phi(\mathbf{X})$  that maps the 5D complex-valued radar cube  $\mathbf{X} \in \mathbb{C}^{2 \times 8 \times 4 \times 4 \times 64 \times 128}$ , where the dimensions correspond to real and imaginary components, time (Table VI), azimuth bins, elevation bins, ADC samples and chirps, into a distribution over the 26 3D pose coordinates  $\hat{\mathbf{y}} \in \mathbb{R}^{26 \times 3}$  using a deterministic encoder and probabilistic decoder. We choose this design to make the model sparse in its computations, while still taking advantage of its probabilistic formalisation.

1) *Preprocessing Block*: The first module in the forward pass removes static clutter by centering the complex radar cube in the chirp dimension and performing a 4D FFT over the ADC sample, chirp, azimuth and elevation dimensions. We follow the approach of [11] and transform our tensor into a coordinate representation where we get a time, Doppler, azimuth, elevation and range tensor  $\mathbf{I} \in \mathbb{C}^{2 \times 8 \times 128 \times 4 \times 4 \times 64}$ .

Therefore, the last three dimensions act as coordinate inputs in 3D space.

2) *Encoder*: Next, we convert the complex tensor to a real tensor by concatenating the real and imaginary parts in the time dimension  $\mathbf{F} \in \mathbb{R}^{16 \times 128 \times 4 \times 4 \times 64}$ . We then use the 3D HRNet backbone network used in Ho et al. [11], adapted from [67], as a feature extraction layer. We use a shared encoder to process the 3D inputs  $\mathbf{F}^t \in \mathbb{R}^{1 \times 128 \times 4 \times 4 \times 64}$  for each time step  $t \in T$ . Since the real and imaginary parts result from mixing the same received signal with orthogonal references [17], they encode structurally similar and complementary information. A shared encoder exploits this similarity for efficient and consistent feature extraction. Therefore, we apply the HRNet backbone to the  $T \times 2$  temporal inputs from the complex tensor (Figure 3) to obtain distinct features for the real and imaginary parts of the input for each time step. The backbone is designed to capture high resolution features throughout the network by branching into parallel features through strided convolutions, halving the spatial dimensions and doubling the channel size at each stage [25]. Finally, the features of different resolutions are upsampled and aggregated for each of the three stages used [11]. In addition, instead of using only the highest resolution representation of the HR backbone [25] for the last stage, we use all representations and upsample and concatenate them in the channel dimension to ensure no information loss. To further reduce the feature size, we apply two 3DConv layers with batch-norm and relu activation functions to reduce the channel dimensions to  $\mathbf{F}^t \in \mathbb{R}^{1 \times 8 \times 4 \times 4 \times 1}$ .

After obtaining  $\mathbf{F}^t$  for each time step, we reshape the features by flattening the spatial dimensions, resulting in  $\mathbf{F} \in \mathbb{R}^{16 \times 128}$ . To capture dependencies between different time steps and spatial locations, we apply self-attention, projecting  $\mathbf{F}$  into queries, keys, and values as

$$\mathbf{Q} = \mathbf{F}\mathbf{W}_Q, \quad \mathbf{K} = \mathbf{F}\mathbf{W}_K, \quad \mathbf{V} = \mathbf{F}\mathbf{W}_V, \quad (7)$$

where  $\mathbf{W}_Q$ ,  $\mathbf{W}_K$ , and  $\mathbf{W}_V$  are learnable projection matrices. The attention output is then computed as

$$\text{Attention}(\mathbf{Q}, \mathbf{K}, \mathbf{V}) = \text{softmax} \left( \frac{\mathbf{Q}\mathbf{K}^\top}{\sqrt{d_k}} \right) \mathbf{V}, \quad (8)$$

where  $d_k$  is the dimensionality of the key vectors. This operation allows each time step to aggregate information from all others, integrating complementary cues from the real and imaginary channels while preserving global temporal context. The attention output is modeled in the standard way with a residual connection,

$$\mathbf{F}' = \mathbf{F} + \text{Attention}(\mathbf{Q}, \mathbf{K}, \mathbf{V}), \quad (9)$$

followed by a linear layer.

Then, we flatten the processed features across the time dimension and fuse them into the latent space through concatenation and linear layers to estimate the mean and dispersion parameters of the latent space distribution.

3) *Latent Space*: We use variational inference to model a distribution over latent variables conditioned on the radar input. Specifically, we evaluate both isotropic Gaussian and

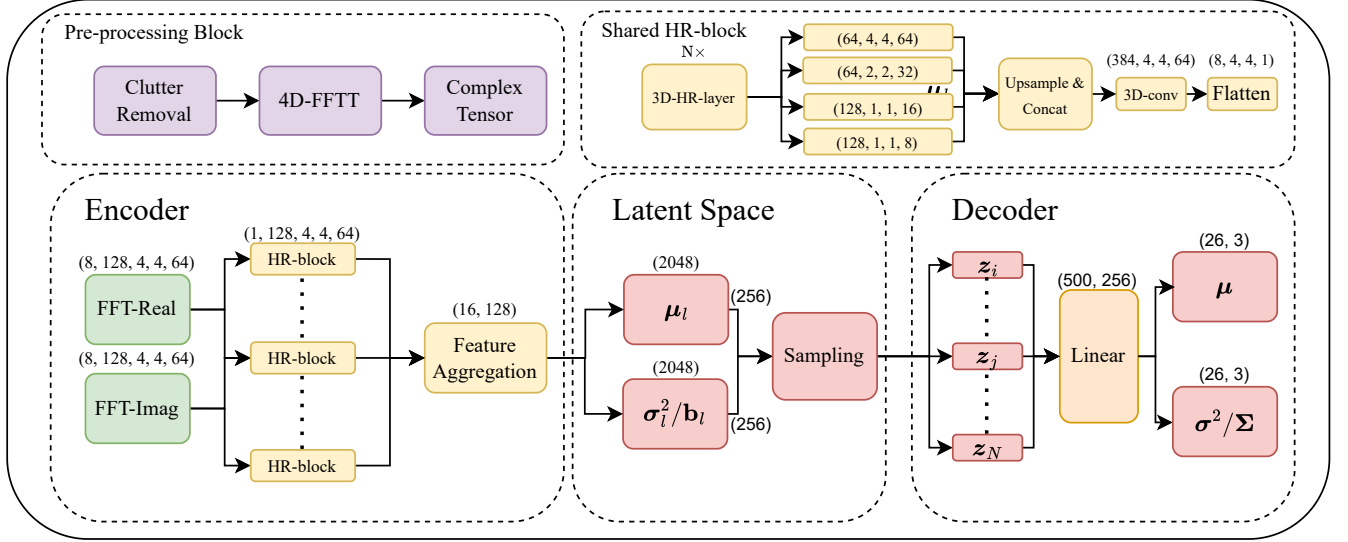


Fig. 3. Overview of the RadProPoser architecture. Bracketed values indicate input tensor dimensions for each processing block. Top left: proposed radar pre-processing pipeline. Top right: adapted HR-block architecture, reused for real and imaginary temporal inputs. Bottom: full forward pass through the network.

Laplacian priors. The encoder outputs the parameters of the latent distribution based on the selected prior

$$\phi(\mathbf{X}) = \begin{bmatrix} \boldsymbol{\mu}_l \\ \log \boldsymbol{\sigma}_l^2 \text{ or } \tilde{\mathbf{b}}_l \end{bmatrix}. \quad (10)$$

The Gaussian latent space distribution is parameterized by a mean vector  $\boldsymbol{\mu}_l$  and log-variance vector  $\log(\boldsymbol{\sigma}_l^2)$ . The KL divergence to the diagonal Gaussian is given by

$$\text{KL}_{\mathcal{N}}(\boldsymbol{\mu}_l, \boldsymbol{\sigma}_l^2) = -\frac{1}{2} (1 + \log \boldsymbol{\sigma}_l^2 - \boldsymbol{\mu}_l^2 - \boldsymbol{\sigma}_l^2), \quad (11)$$

where  $\boldsymbol{\mu}_l$  and  $\boldsymbol{\sigma}_l^2 \in \mathbb{R}^{256}$ . To encourage a sharp latent distribution, which influences the sharpness of the output distribution, we introduce a learnable global scaling factor  $\alpha$  that adjusts the sampling variance. Latent vectors are sampled as

$$\mathbf{z}_i = \boldsymbol{\mu}_l + \alpha \boldsymbol{\epsilon}_i \boldsymbol{\sigma}_l, \quad \boldsymbol{\epsilon}_i \sim \mathcal{N}(0, \mathbf{I}), \quad (12)$$

where  $i \in N$  indexes the samples.

The Laplacian latent space distribution is parameterized by a mean  $\boldsymbol{\mu}$  and a positive scale parameter vector  $\mathbf{b}$ . To ensure numerical stability and enforce positivity, we apply the softplus function to the raw scale output

$$\mathbf{b}_l = \text{softplus}(\tilde{\mathbf{b}}_l), \quad (13)$$

where  $\tilde{\mathbf{b}} \in \mathbb{R}^{256}$  is an unconstrained output of the encoder. Latent samples are drawn as

$$\mathbf{z}_i \sim \mathcal{L}(\boldsymbol{\mu}_l, \mathbf{b}_l), \quad (14)$$

without additional scaling, since the Laplace distribution inherently yields sharper samples than the Gaussian case. Backpropagation is implemented with the reparameterization trick via inverse cumulative distribution sampling [68].

4) *Decoder*: The decoder computes the output distribution

$$\Theta(\mathbf{z}) = \hat{\mathbf{y}}, \quad (15)$$

where  $\Theta$  is a simple two-layer linear network,  $\mathbf{z}$  is a matrix  $\in \mathbb{R}^{500 \times 256}$ , and  $\hat{\mathbf{y}} \in \mathbb{R}^{500 \times 78}$ . To train the models we then compute mean  $\boldsymbol{\mu}$  and variance vectors  $\boldsymbol{\sigma}^2 \in \mathbb{R}^{78}$  from these predictions to optimize our loss functions, where their index  $d$  represents a specific dimension for a specific keypoint. If we assume correlation between output dimensions we compute a covariance matrix  $\boldsymbol{\Sigma} \in \mathbb{R}^{78 \times 78}$  instead of variance vector. We then reshape the predictions from  $78$  to  $26 \times 3$  to get the 3D keypoints, respectively. Therefore, the encoder can be deterministic while we exploit the probabilistic nature of the small decoder to decrease computation time. Note that storing the samples in the batch dimension allows us to get the full output distribution with one parallel forward pass.

5) *Loss functions*: In summary, based on our formulations in Section II, we can now formalize the full loss for the Gaussian case as

$$\mathcal{L} = \text{NLL}(\mathbf{y}, \boldsymbol{\mu}, \boldsymbol{\sigma}^2) + \beta \text{KL}(\boldsymbol{\mu}_l, \boldsymbol{\sigma}_l^2), \quad (16)$$

where

$$\text{NLL}(\mathbf{y}, \boldsymbol{\mu}, \boldsymbol{\sigma}^2) = \frac{\|\mathbf{y} - \boldsymbol{\mu}\|_2^2}{\boldsymbol{\sigma}^2} + \gamma \sum_{i=1}^d \log(\boldsymbol{\sigma}_i^2), \quad (17)$$

which is derived from equation 5 in [43], ignoring constants in the optimization process, where  $d$  is the data dimensionality. For the multivariate Gaussian with non-diagonal covariance matrix [42], we can extend this formulation to

$$\text{NLL}(\mathbf{y}, \boldsymbol{\mu}, \boldsymbol{\sigma}^2) = \gamma \sum_{i=1}^N \log |\boldsymbol{\Sigma}_{\boldsymbol{\theta}}(\mathbf{x}_i)| + (\mathbf{y}_i - \boldsymbol{\mu}_{\boldsymbol{\theta}}(\mathbf{x}_i))^\top \boldsymbol{\Sigma}_{\boldsymbol{\theta}}^{-1}(\mathbf{x}_i) (\mathbf{y}_i - \boldsymbol{\mu}_{\boldsymbol{\theta}}(\mathbf{x}_i)) \quad (18)$$

For the Laplacian case, the loss function boils down to

$$\text{NLL}(\mathbf{y}, \boldsymbol{\mu}, \mathbf{b}) = \frac{|\mathbf{y} - \boldsymbol{\mu}|}{\mathbf{b}} + \gamma \sum_{i=1}^d \log(2\mathbf{b}_i) \quad (19)$$

For all loss functions one term encourages the model to trade off accuracy for uncertainty, while the other acts as a regularizer [43] to learn sharp predictive distributions.

#### IV. EXPERIMENTS

##### A. Baseline Models and Performance Metrics

RadProPoser is trained to predict 26 three-dimensional keypoints from raw radar tensors, supervised by OMC data. The data is split by participant to encourage generalization across body types. Three participants are held out for testing, one is used for hyperparameter tuning, and eight are used for training. After tuning, each model is retrained on the full set of nine training participants. Based on a parameter sensitivity analysis conducted on RadProPoser, we converge on an input sequence of eight radar frames, corresponding to approximately half a second of temporal context. This choice balances temporal information content with robustness to noise. All non-probabilistic baselines are trained using mean squared error loss, and all but one single-frame baseline adopt this temporal window. We evaluate three non-probabilistic baselines and two probabilistic variants designed to capture predictive uncertainty.

The three non-probabilistic baselines are evaluated alongside RadProPoser. Our architecture extends the HRNet encoder of Ho *et al.* [11], the only prior method that uses a single radar and the full complex-valued tensor for three-dimensional pose estimation. As the first baseline we adapt their classification output for the root joint to a regression task by regressing the root joint and relative offsets. The original model proposes single-frame processing to reduce the memory and computational load of complex-valued radar tensors. Since our radar is notably smaller, the second baseline is a CNN-LSTM that processes sequences of radar frames with our modified HRNet encoder followed by a temporal LSTM regression head, inspired by prior range-Doppler work [9], [8]. The third baseline is our previous point cloud model [64] retrained under the same data split. The method of Lee *et al.* [7], which employs two radars and produces two-dimensional image-space keypoints, is excluded because it is incompatible with our setup.

Two probabilistic variants extend the RadProPoser encoder to model predictive uncertainty. The evidential regression variant [69] augments the decoder to output the parameters of a normal-inverse-gamma distribution, yielding a Student *t* predictive distribution under the deep evidential regression framework [69], [33]. This formulation allows for the direct quantization of aleatoric uncertainty. The second variant uses the RPP encoder and replaces the Gaussian latent space with a RealNVP normalizing flow [70]. RealNVP is selected because it introduces few assumptions about the latent distribution and its transformations, the flow model, or the data, allowing the model to capture more complex radar-to-pose mappings and to estimate total uncertainty, compared to explicit aleatoric

prediction. The training loss includes an MSE term between a single pose prediction sample and the ground truth, combined with a scaled KL-divergence regularization term derived from the change-of-variable formula [71]. During inference, multiple latent samples are drawn to construct the predictive distribution. Implementation details and all hyperparameter configurations are provided in the accompanying GitHub repository.

We measure pose accuracy [15] using the commonly used MPJPE, defined as

$$\text{MPJPE}_k = \frac{1}{N} \sum_{i=1}^N \|\hat{\mathbf{y}}_{i,k} - \mathbf{y}_{i,k}\|_2, \quad (20)$$

where  $k$  denotes the keypoint index and  $i$  the sample index. Additionally, we report the Procrustes-aligned MPJPE (P-MPJPE), which applies Procrustes analysis to align the predicted and ground truth skeletons using a least-squares rigid transformation (translation, rotation, and scaling). This alignment isolates structural pose accuracy independent of global positioning.

Furthermore, we quantify predictive uncertainty for each keypoint by summing the predicted variances over the three spatial dimensions

$$\mathbf{u}_k = \sum_{d=1}^3 \sigma_{k,d}^2. \quad (21)$$

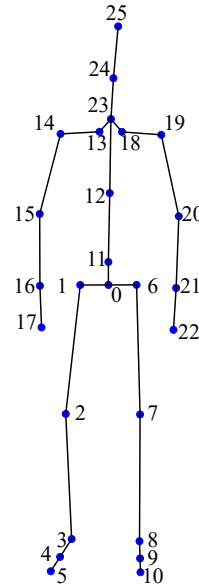


Fig. 4. Skeleton keypoint structure.

## V. RESULTS

### A. Human Pose Estimation

We can see that the models trained with Gaussian Log-likelihood achieve the lowest errors based on the MPJPE and procrustes-aligned MPJPE (Table III). The RPP-Gauss.-Gauss.-Cov model achieves the lowest overall average MPJPE

TABLE III  
AVERAGE MEAN PER-JOINT POSITION ERROR  $\downarrow$  OF THREE TEST-SET PARTICIPANTS FOR THE THREE RECORDED ANGLES IN CM.

Model	MPJPE (0°)			MPJPE (45°)			MPJPE (90°)			Avg. MPJPE			Overall Avg.
	P12	P2	P1										
<b>Baselines</b>													
Ho et al. [11]	10.881	8.700	5.946	6.476	6.208	7.438	6.481	6.544	7.945	7.946	7.151	7.110	7.402
Engel et al. [64]†	11.527	8.318	6.643	6.108	6.829	7.662	6.733	7.503	9.695	8.186	7.609	8.031	7.946
Evidential regression	13.522	12.732	11.285	9.632	11.396	11.086	9.923	11.562	11.396	11.026	11.897	11.256	11.393
<b>RPP Variants (ours)</b>													
RPP-CNN-LSTM	9.906	7.818	5.397	5.774	<b>5.557</b>	6.820	6.170	6.443	7.747	7.707	<b>6.050</b>	6.787	6.848
RPP-Normalizing-Flows	<b>7.417</b>	7.632	7.097	5.788	6.085	7.023	6.639	6.941	7.196	6.947	6.886	7.072	7.022
RPP-Gauss.-Gauss.-Cov.	9.369	<b>7.228</b>	<b>5.027</b>	<b>4.922</b>	5.849	<b>6.264</b>	5.635	6.307	7.220	<b>6.642</b>	6.461	<b>6.170</b>	<b>6.425</b>
RPP-Gauss.-Gauss.	9.970	8.028	5.127	5.556	5.710	6.374	<b>5.581</b>	<b>6.001</b>	<b>7.022</b>	7.036	6.580	6.174	6.597
RPP-Laplace-Laplace	9.988	9.061	7.783	5.591	6.665	7.098	5.683	6.949	7.321	7.087	7.558	7.401	7.349
RPP-Laplace-Gauss.	9.063	7.641	5.203	5.202	5.975	6.583	5.763	6.568	7.166	6.676	6.728	6.317	6.688
RPP-Gauss.-Laplace	10.777	9.491	7.014	5.813	7.015	7.320	6.007	7.163	8.126	7.532	7.890	7.487	7.592

The Models are presented as RPP-[Latent Prior]-[Log-likelihood]. † Pointcloud-based approach.

TABLE IV  
PROCRUSTES ALIGNED MEAN PER-JOINT POSITION ERROR  $\downarrow$  OF THREE TEST-SET PARTICIPANTS FOR THE THREE RECORDED ANGLES IN CM.

Model	P-MPJPE (0°)			P-MPJPE (45°)			P-MPJPE (90°)			Avg. P-MPJPE			Overall Avg.
	P12	P2	P1	P12	P2	P1	P12	P2	P1	P12	P2	P1	
<b>Baselines</b>													
Ho et al. [11]	5.939	6.048	4.524	4.249	4.540	5.559	5.097	5.427	6.315	5.095	5.339	5.466	5.300
Engel et al. [64]†	<b>5.122</b>	<b>5.384</b>	4.521	4.132	4.638	5.625	5.156	5.797	7.762	4.803	5.273	5.969	5.348
Evidential Regression	10.417	12.130	9.576	9.346	11.718	10.394	9.989	12.118	10.709	9.917	11.989	10.226	10.711
<b>RPP Variants (ours)</b>													
RPP-CNN-LSTM	6.018	6.819	4.928	4.499	5.425	6.346	5.386	5.626	6.620	5.301	5.957	5.965	5.741
RPP-Normalizing-Flows	6.264	7.028	5.168	4.363	5.503	6.424	5.368	6.082	6.725	5.665	6.204	6.106	6.325
RPP-Gauss.-Gauss.	5.939	6.389	4.764	3.948	4.608	5.290	4.900	5.423	<b>5.793</b>	4.929	5.473	5.282	5.228
RPP-Gauss.-Gauss.-Cov.	5.363	5.516	<b>3.970</b>	<b>3.738</b>	<b>4.128</b>	<b>5.074</b>	<b>4.654</b>	<b>4.797</b>	5.918	<b>4.585</b>	<b>4.813</b>	<b>4.987</b>	<b>4.795</b>
RPP-Laplace-Laplace	6.601	7.396	5.116	4.374	5.152	5.807	4.870	5.938	6.287	5.282	6.162	5.737	5.727
RPP-Laplace-Gauss.	5.772	6.050	4.237	3.980	4.250	5.416	4.865	5.377	5.942	4.872	5.226	5.198	5.099
RPP-Gauss.-Laplace	6.927	7.950	5.131	4.692	5.680	6.155	5.238	6.186	6.841	5.619	6.605	6.042	6.200

The Models are presented as RPP-[Latent Prior]-[Log-likelihood]. † Pointcloud-based approach.

of 6.425 cm across all test participants and viewing angles, followed by the RPP-Gauss.-Gauss. model with MPJPE of 6.597 cm and the RPP-Laplace-Gauss. model with 6.688 cm. The CNN-LSTM baseline performs comparably, with a slightly higher average MPJPE of 6.848 cm, followed by the RPP-Laplace-Gauss model at 6.893 cm, the Normalizing FFlow model 7.022 cm and the RPP-Laplace-Laplace variant at 7.349 cm. The RPP-Gauss.-Laplace configuration yields the highest error among our probabilistic variants, with an overall MPJPE of 7.592 cm. For comparison, the baseline from Ho et al. [11] reports an MPJPE of 7.110 cm, while the point cloud-based method by Engel et al. [64] results in an error of 8.031 cm. The 45° angle condition results in the best accuracy across all models. In this condition, the RPP-Gauss.-Gauss.-Cov. model achieves an average MPJPE of 5.678 cm. The Procrustes-aligned (Table V) mean per-joint position error (P-MPJPE) reveals a similar performance trend across models, albeit with reduced absolute differences between models. Thus, the models trained with Gaussian Log-likelihood consistently show the lowest P-MPJPE, especially the variant with full covariance used for training. Notably, the point cloud-based method by Engel et al. and the single-frame approach by Ho et al. now perform better compared to the proposed RPP-based models under alignment.

We additionally conduct a parameter sensitivity analysis to

assess the influence of the latent space size and the temporal context window (Table VI). Increasing the latent dimensionality or reducing the time interval does not yield better accuracy. Based on this analysis, we select a latent size of 256 and a time interval of  $t = 8$  for the final model configuration.

### B. Uncertainty Analysis

Additionally, we are interested in the learned uncalibrated uncertainties of our best performing model to uncover patterns of hard-to-recover keypoints. Table V and Figure 4 give an overview of the uncertainties and associated errors averaged over the whole test-set. We can observe that some keypoints, especially the ones with low reflection surfaces like the head, hands (wrists), the hand-ends, or the forearms, show higher errors and uncertainties. We observe a similar, but smaller, effect for the legs. Additionally, we see a slight increase in MPJPE and uncertainties for the left arm keypoints compared to the right arm keypoints, especially for the hand (RPP:  $\Delta$ MPJPE = 2.172 cm) and hand-end joints (RPP:  $\Delta$ MPJPE = 3.418 cm).

A known challenge for probabilistic deep learning models is that they may produce predictive distributions that are overconfident or underconfident, failing to accurately reflect the true data-generating process [49], [41]. Consequently, a calibration analysis of the predictive distributions is essential

TABLE V  
AVERAGE MEAN PER-JOINT POSITION ERRORS (MPJPE) IN CM ↓, UNCALIBRATED UNCERTAINTIES, AND CALIBRATED UNCERTAINTIES (TOTAL VARIANCE ACROSS KEYPOINT DIMENSIONS), GROUPED BY BODY PARTS.

Body Center						
Keypoint	Hips (0)	Spine (11)	Spine1 (12)	Neck (23)	Head (24)	HeadEnd (25)
MPJPE	4.288	4.242	4.527	4.850	6.149	9.837
Uncalibrated Uncertainty	3.095	3.062	3.034	4.133	5.450	10.174
Calibrated Uncertainty	17.115	16.798	16.877	22.765	33.385	64.218
Right Leg						
Keypoint	RightHip (1)	RightKnee (2)	RightHeel (3)	RightFootCenter (4)	RightFootEnd (5)	
MPJPE	4.610	4.885	5.674	5.822	5.903	
Uncalibrated Uncertainty	3.215	4.435	3.760	3.798	4.097	
Calibrated Uncertainty	17.909	18.180	22.137	22.276	23.733	
Left Leg						
Keypoint	LeftHip (6)	LeftKnee (7)	LeftHeel (8)	LeftFootCenter (9)	LeftFootEnd (10)	
MPJPE	4.271	5.551	4.580	5.317	5.628	
Uncalibrated Uncertainty	3.347	4.836	4.010	3.934	4.197	
Calibrated Uncertainty	18.223	31.679	19.219	28.167	30.742	
Right Arm						
Keypoint	RightNeck (13)	RightShoulder (14)	RightForeArm (15)	RightHand (16)	RightHandEnd (17)	
MPJPE	4.862	6.270	7.993	9.600	11.658	
Uncalibrated Uncertainty	3.791	4.626	8.568	10.602	16.637	
Calibrated Uncertainty	20.879	23.096	47.218	66.751	140.036	
Left Arm						
Keypoint	LeftNeck (18)	LeftShoulder (19)	LeftForeArm (20)	LeftHand (21)	LeftHandEnd (22)	
MPJPE	4.765	5.514	8.448	11.772	15.076	
Uncalibrated Uncertainty	3.885	4.798	9.949	12.564	19.548	
Calibrated Uncertainty	21.620	23.400	56.992	89.680	169.899	

TABLE VI  
PARAMETER SENSITIVITY ANALYSIS ON THE BEST PERFORMING RADPROPOSER MODEL

Condition	MPJPE (cm)
$t = 2, d_{\text{lat}} = 256$	7.357
$t = 4, d_{\text{lat}} = 256$	7.215
$t = 8, d_{\text{lat}} = 256$	6.425
$d_{\text{lat}} = 512, t = 8$	6.961
$d_{\text{lat}} = 1024, t = 8$	7.332

t: time interval,  $d_{\text{lat}}$ : latent space dimensionality

(Figure 5). In regression, a distributional predictor is calibrated if

$$\frac{1}{N} \sum_{n=1}^N \mathbf{1}\{y_n \leq F_n^{-1}(p)\} \rightarrow p, \quad \forall p \in [0, 1] \quad (22)$$

as  $N \rightarrow \infty$ .  $F_n^{-1} : [0, 1] \mapsto \mathcal{Y}$  is the quantile function conditioned on sample  $n$ . To assess and correct calibration empirically, we employ the approach of Kuleshov et al. [49], computing the empirical coverage of prediction intervals across different confidence levels (Table VII). We first evaluate the raw predictive distributions on two of the three test participants by computing, for each expected coverage rate  $p \in [0, 1]$ , the fraction of true keypoint positions that fall below the predicted  $p$ -th quantile across all test samples. Perfect calibration would yield a diagonal relationship between expected coverage and empirical coverage. We then use the data from one held-out test participant to recalibrate the predictive distributions. Subsequently, we evaluate the recalibrated distributions on the remaining two test participants to assess generalization performance (Table 5).

A well-calibrated model is not sufficient on its own because it must also demonstrate sharpness by producing confident predictions when appropriate. A model that generates overly wide prediction intervals may still be calibrated, but it offers limited practical value due to its lack of specificity. To comprehensively assess the quality of the recalibrated predictive distributions, we evaluate both the expected calibration error (ECE) [49] and the sharpness criterion. Calibration error is computed as

$$\text{ECE} = \frac{1}{c} \sum_{j=1}^c \left| \hat{P}(p_j) - p_j \right|, \quad (23)$$

where  $\hat{P}(p_j) = \frac{1}{N} \sum_{i=1}^N \mathbf{1}(u_i \leq p_j)$  is the empirical frequency of predicted CDF values below each target level  $p_j$ . We use the L1 norm here to make the differences of the errors more visible.

We define the sharpness score as the mean predicted variance across all keypoints and dimensions. Let  $\sigma_i^2$  denote the predicted variance for keypoint  $k$  across all test-set samples. The sharpness is defined as the average uncertainty across keypoints and test-set datapoints

$$\text{Sharpness} = \frac{1}{NK} \sum_{k=1}^K \sum_{i=1}^N \sigma_{i,k}^2. \quad (24)$$

Our initial analysis reveals that the models exhibit moderate miscalibration, with a tendency toward overconfidence in high-certainty predictions (Table 5). The Normalizing Flow model exhibits the best uncalibrated calibration with ECE of 0.078, followed by the RPP Gauss.-Gauss.-Cov. variant with ECE of 0.140. To address this, we fit an isotonic regression model on the one held out test participant to learn a recalibration

TABLE VII  
CALIBRATION AND SHARPNESS IN  $CM^2$  ACROSS MODELS

Model	Uncalibr. ECE	Calibr. ECE	Uncalibr. Sharp.	Calibr. Sharp.
RPP-Gauss.-Gauss-Cov.	0.140	0.027	6.290	40.884
RPP-Gauss.-Gauss.	0.163	0.031	2.146	16.871
RPP-Laplace-Gauss.	0.171	0.022	1.938	12.964
RPP-Gauss.-Laplace	0.185	0.021	1.532	14.771
RPP-Laplace-Laplace	0.154	0.026	8.970	58.372
RPP-Normalizing Flows	0.078	0.044	28.623	57.061
Evidential Regression	0.180	0.042	9054.15	4906.734

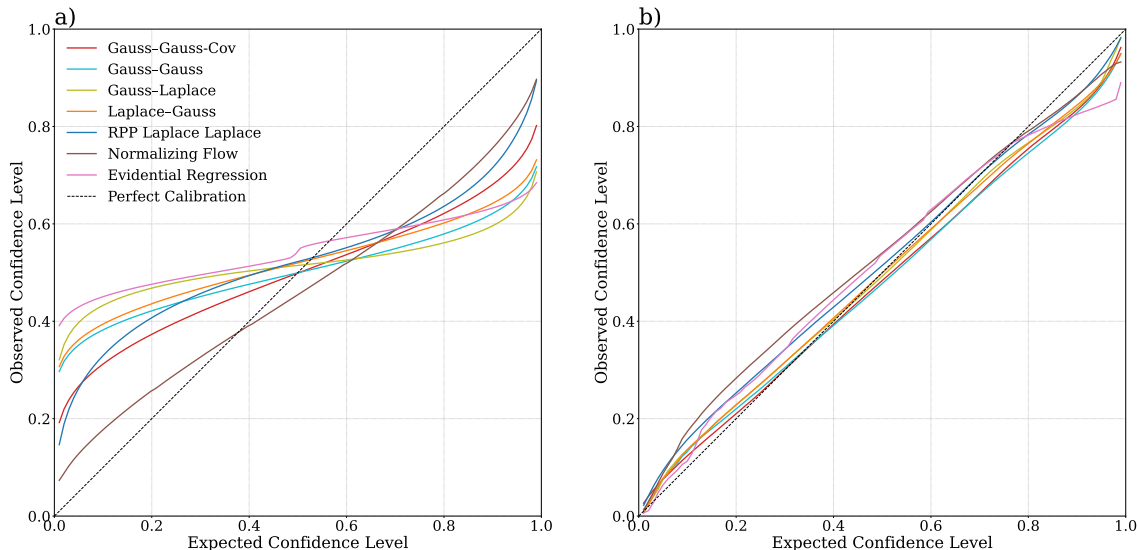


Fig. 5. Calibration performance of all RadProPoser models shown as a function of expected confidence. a) Uncalibrated Models, b) Calibrated Models. The models are defined as [Prior]-[Likelihood].

mapping  $R : [0, 1] \rightarrow [0, 1]$  between predicted and empirical coverage probabilities. This learned mapping is then applied to transform the predicted distributions for the remaining unseen test samples, ensuring that the recalibrated confidence levels accurately reflect empirical coverage rates. The effectiveness of this recalibration is subsequently evaluated, demonstrating improved alignment between predicted and actual coverage probabilities (Figure 5). All RPP variants exhibit comparable performance, while consistently achieving lower ECE scores than the baseline methods. The Laplace-Gauss. variant achieves the best calibrated ECE with 0.021. After recalibration the predictive distributions are no longer symmetric. We therefore estimate each calibrated variance by numerical integration of the quantile function to get the sharpness values, following

$$\hat{\sigma}_k^2 = \int_0^1 (Q_k(p) - m_k)^2 dp, \quad (25)$$

where

$$Q_k(p) = F_{\text{cal},k}^{-1}(p), \quad m_k = \int_0^1 Q_k(p) dp.$$

Among all RPP variants, the RPP-Laplace-Laplace model yields the highest calibrated sharpness, which can be attributed to the characteristic sharp peak and heavy tails of the Laplace distribution. The Normalizing Flow and Evidential Regression models exhibit the highest overall sharpness values. For the Normalizing Flow model, this is due to its greater expressive capacity, while in the case of Evidential Regression, it results from extremely long-tailed uncertainty estimates for specific keypoints, e.g.  $\sigma_{\text{right-hand}}^2 = 65005.278$ .

### C. Latent Space Analysis

Figure 6 visualizes the learned latent representations of different exercises on the training set using t-SNE dimensionality reduction. The embeddings reveal distinct clustering patterns across participants and activities, indicating that the model effectively captures structure in the data. To further assess the utility of the learned representations, we train activity classification models using encoded latent distribution sequences over whole exercises on the train-set. Training data is augmented by sampling from these distributions with variability controlled by the  $\alpha$  parameter in gaussian latent

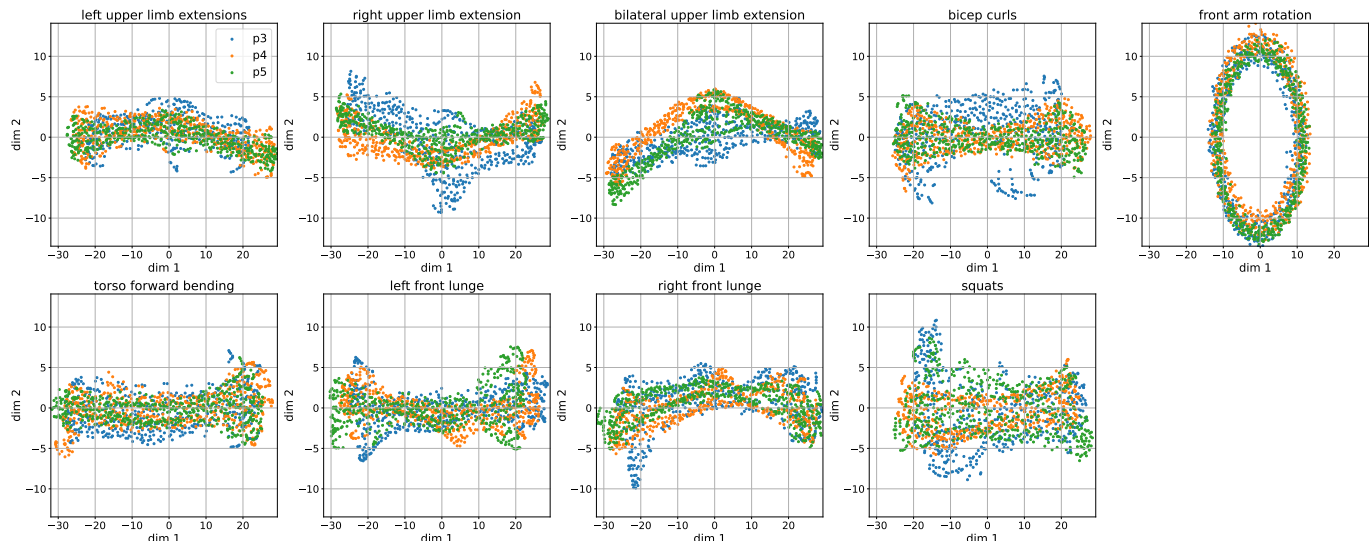


Fig. 6. t-SNE dimensionality reduced latent space representations for all exercises for three participants of the train set

space, as defined in Equation 12. For evaluation, a single sample is drawn from each testset exercise sequence. The classification architecture consists of a 1D convolutional neural network that compresses the latent dimensionality from 256 to 64, applies average pooling over the temporal axis, and uses a fully connected layer to predict logits. Sequence padding is employed to address variable-length inputs. To isolate the effect of augmentation, we compare this model to an identical architecture trained on non-augmented data, where each latent sequence is represented by its mean (i.e.,  $z = \mu$ ). Augmented training involves generating 100 samples per sequence for each participant using 11 distinct  $\alpha$  values, 10 sampled uniformly from the interval  $0.0129 \pm 0.01$  and the originally learned value  $\alpha = 0.0129$ . The augmented model achieves markedly better performance, with an F1 score of 0.870, precision of 0.891, recall of 0.852, and accuracy of 0.852. In contrast, the non-augmented model attains an F1 score of 0.657, precision of 0.688, recall of 0.627, and accuracy of 0.630. As illustrated in Figure 7, misclassifications are more frequent for movements involving fine arm gestures and complex, multi-joint coordination, highlighting the challenges posed by these activity types.

## VI. DISCUSSION

This study applies variational inference modeling to radar-based HPE, achieving state-of-the-art results [11], [8], [7] on a new dataset with high-accuracy OMC ground truth data. Our best performing model, using a Gaussian latent space and multivariate log-likelihood for training, achieves an average MPJPE of 6.425 cm across all exercises, angles, and test participants and 5.678 cm under the optimal radar angle of  $45^\circ$ , while also providing uncertainty estimates that reflect data-driven challenges in keypoint regression. By using minimally processed raw radar data, we avoid information loss from pre-processing algorithms, while ensuring cost-effective scalability through the use of a radar sensor with a small antenna array.

Beyond keypoint estimation, our model learns informative latent space distributions (Figure 6) that support uncertainty

Left upper limb extension	1.00	0.00	0.00	0.00	0.00	0.00	0.00	0.00	0.00
Right upper limb extension	0.00	0.67	0.33	0.00	0.00	0.00	0.00	0.00	0.00
Bilateral upper limb extension	0.00	0.00	1.00	0.00	0.00	0.00	0.00	0.00	0.00
Bicep curls	0.00	0.00	0.00	1.00	0.00	0.00	0.00	0.00	0.00
Front arm rotation	0.00	0.00	0.33	0.00	0.67	0.00	0.00	0.00	0.00
Torso forward bending	0.00	0.00	0.00	0.00	0.00	1.00	0.00	0.00	0.00
Left front lunge	0.00	0.00	0.00	0.00	0.00	0.33	0.67	0.00	0.00
Right front lunge	0.00	0.00	0.00	0.00	0.00	0.00	0.00	1.00	0.00
Squats	0.00	0.00	0.00	0.00	0.33	0.00	0.00	0.00	0.67
Left upper limb extension									
Right upper limb extension									
Bilateral upper limb extension									
Bicep curls									
Front arm rotation									
Torso forward bending									
Left front lunge									
Right front lunge									
Squats									

Fig. 7. Normalized confusion matrix of our proposed activity classification model.

quantification. The regressed aleatoric uncertainties show strong alignment with prediction errors and can be recalibrated to reflect total uncertainty, including both aleatoric and epistemic components. The latent space also enables generative modeling for training downstream activity classifiers. The alignment between uncertainty and estimation error indicates the model’s capacity to capture keypoint-specific ambiguity, while the latent representations effectively encode movement patterns, as reflected in activity classification performance.

### A. Human Pose Estimation

A central question in our setup is whether the output keypoint dimensions can be adequately modeled as independent [39], or whether a structured multivariate distribution is necessary [42]. Our results indicate consistent performance gains when employing a full covariance structure in the training process, leading to lower pose estimation errors compared to the independence assumption. This outcome aligns

with the physical properties of the human kinematic chain, which exhibits strong spatial dependencies between joints and temporal correlations due to its constrained range of motion and invariant structural relationships [72]. Calibration analysis corroborates these findings, showing that the full-covariance model achieves second best uncalibrated ECE, with the only exception being the normalizing flow variant, which slightly outperforms it due to its more flexible latent space.

We compare RadProPoser to a range of baselines, including the single-frame model by Ho *et al.* [11], which, to our knowledge, is the only method in the literature that uses the full complex-valued radar tensor from a single radar for HPE. Models incorporating a wider temporal window, such as RadProPoser or our CNN-LSTM variant, outperform this baseline on our dataset by capturing motion context beyond a single radar frame [11]. This difference is less pronounced for P-MPJPE, suggesting, that extending the radar cube with temporal information enhances robustness to translation and scaling artifacts. Nonetheless, it should be mentioned that this result reflects our implementation of the model, based on our different ground-truth and radar data. On the other hand, these findings are consistent with other radar-based pose estimation pipelines that successfully leverage multi-frame inputs [7], [8]. While multi-frame processing increases memory demands, especially with large antenna arrays, our sparse radar design can enable efficient batched processing of temporal input sequences. Temporal features can be extracted in a causal online inference setting by applying the shared encoder independently (Figure 3) to the stacked real and imaginary components of the time steps along the batch dimension. This setup enables a single parallel forward pass across the sequence, followed by parallel decoding to get the predictive distribution. As a result, the model can ingest full radar tensors from eight consecutive frames without introducing significant computation time overhead, preserving the benefits of temporal context while maintaining low inference latency, especially given modern GPU hardware.

The CNN-LSTM baseline, which explicitly models temporal dependencies through recurrent updates, achieves performance close to RadProPoser. However, its marginal performance difference suggest that recursive fusion of temporal features does not provide additional benefit in our setting. In contrast, RadProPoser integrates temporal and spatial information directly into the latent space, regulated by a KL-penalty for Gaussian models or sharp Laplacian priors, which stabilizes training and avoids vanishing or exploding gradients.

The Normalizing Flow model demonstrates consistent performance across participants and viewing angles, likely due to its expressive latent space, which can better capture complex radar-to-pose relationships. However, RadProPoser with a Gaussian latent space generally performs better when the radar input is more informative, such as under favorable view conditions, though it exhibits slightly higher variability. This suggests that, although Normalizing Flows provide robust performance across viewing angles, RadProPoser’s structured latent modeling yields higher accuracy, especially under favorable side-view conditions. In our experiments, the evidential regression model achieves lower pose estimation

accuracy compared to other models. This may suggest that its underlying distributional assumptions, while effective in other domains [73], are not fully aligned with the statistical properties of radar-based pose estimation, reflected in high outliers in uncertainty attribution.

Finally, our results across models indicate that the 45° and 90° conditions, where the subject is oriented at an angle or side view relative to the radar, yield the most consistent performance, with relatively uniform prediction errors across participants. In contrast, the 0° condition, where the subject directly faces the radar, exhibits greater variability. This is likely due to reduced visibility of lateral body parts, such as the arms and hands, which are more clearly resolved at oblique angles due to a richer reflectance spectrum. We also observe a systematic asymmetry in keypoint prediction errors between the left and right arms, with higher errors and uncertainties on the left. This can be attributed to the recording setup, where participants were rotated 45° and 90° counterclockwise, resulting in more frequent exposure of the right side to the radar. These findings suggest that increasing the radar visibility of specific joints can reduce uncertainty and improve performance, and that future applications should prioritize side-angle views to enhance accuracy and consistency.

### B. Insights from Uncertainty Modeling

A key contribution of our work is the integration of learned aleatoric uncertainties into keypoint prediction. We therefore analyse the keypoints associated with smaller reflective surfaces, such as the hands, forearms, or head for our best performing model in the pose estimation task the RPP-Gauss.-Gauss.-Cov. variant. These keypoints exhibit higher uncertainties and errors, in line with the higher reported errors in radar-based HPE of these areas [9], [11], [7]. This is probably due to weaker signal reflections and higher noise levels for these joints in the radar-cube data. Therefore, we can now quantify these effects in a data-driven manner and use uncertainty predictions for applications. Notably, the higher errors for these joints persist even with larger radar arrays [11], suggesting that it is an inherent attribute of radar-based HPE. By modeling irreducible noise through aleatoric uncertainty and using accurate ground truth with raw radar data, our results support a data-driven explanation for the higher errors and uncertainties due to the inherent ambiguity in the radar signal for these keypoints. This conclusion is underlined by the asymmetry of the prediction accuracies and uncertainties between the two body sides.

After isotonic recalibration, most models exhibit strong calibration performance, closely matching the empirical data distribution (Table 5). Among them, the RPP variants trained with a Laplacian likelihood or latent prior yield the best recalibrated uncertainty estimates, although differences to models like the Gaussian variants are marginal. This can be attributed to the well-defined structure of the Laplace, the Gaussian or the Multivariate Gaussian output distribution, which enables straightforward and effective recalibration of predictive quantiles. Although initially overconfident, these RPP variants achieve much lower calibration error post-recalibration,

demonstrating suitability for producing trustworthy and informative uncertainty estimates. We additionally observe that both uncalibrated and calibrated uncertainties are higher for the RPP model when trained with a full Gaussian covariance matrix compared to the independent (diagonal) case. This indicates that explicitly modelling variability and correlations between output dimensions improves performance [43], and supports the conclusion that such a modelling choice is both reasonable and necessary, as reflected in the respective increase in predicted uncertainties.

Among the uncalibrated models, the Normalizing Flow baseline attains the lowest calibration error. Its expressive, invertible latent transformation approximates the full predictive distribution and therefore captures input-dependent total uncertainty directly. RadProPoser and the evidential regression variant, in contrast, are trained only for the aleatoric component and convert it to total uncertainty through a subsequent quantile-based recalibration step. Using Normalizing Flows in the latent space with our setup thus offer superior “off-the-shelf” calibration when only the aggregate uncertainty is of interest. However, because the used flow model [71] conflates aleatoric and epistemic sources to get more expressiveness, it does not directly reveal how much uncertainty is aleatoric or epistemic. Other recent approaches estimate aleatoric and epistemic uncertainties for Normalizing Flows directly on toy benchmark datasets, where the latent base distribution is used for aleatoric uncertainty prediction [74]. Thereby RadProPoser is a special case of this model using only the base distribution for aleatoric uncertainty and can be upgraded with Normalizing Flows or a recalibration model to also obtain epistemic and total uncertainty. Our two-stage strategy for RPP, first learning aleatoric uncertainty, and then extends it to total uncertainty via recalibration, thus preserves interpretability and yields the best overall pose estimation and recalibration results for RPP in our setup.

Future work will now use our method to collect additional motion data, focusing on keypoints with the highest predicted uncertainties. By targeting these uncertain regions, we aim to reduce model uncertainty and error during subsequent fine-tuning or retraining. Furthermore, the learned uncertainty distributions can guide the generation of synthetic data. For example, ray-tracing techniques [75], [76] can simulate radar data sampled according to these uncertainties, allowing for more efficient data generation compared to random sampling or domain randomization [77]. To further optimize performance across different environments, we also plan to investigate the impact of various radar configurations, using uncertainty modeling to empirically assess the limitations and robustness of specific sensor setups.

As uncertainty modeling is well established in biomechanics [78], we also aim to incorporate the estimated uncertainties into musculoskeletal simulations, bridging radar-based HPE with physiologically detailed physics-based motion modeling [72] to reconstruct the uncertain parts of our predictions from physics. Biomechanical simulations with sensor data [79], such as optical motion capture or inertial measurement units [80], are typically operationalized as motion reconstruction minimizing an additional physics-based loss term. Here we

can now directly use our learned uncertainties in the loss equations to rely more on simulation-based reconstruction for hard examples and keypoints on a sample-by-sample basis. These extensions could help to refine radar-based human motion analysis by exploiting both data-driven and biomechanical constraints to increase the applicability of radar-based pose estimation to more use cases. In addition, we plan to incorporate belief propagation techniques to enhance our temporal pose estimation framework, for example by using Kalman Filters [81]. Belief propagation can naturally integrate our model’s uncertainty estimates across the temporal window, enabling more principled information fusion during for example partial occlusions by automatically weighting contributions from high-confidence frames while downweighting occluded observations, thereby propagating uncertainties through time.

### C. Activity Classification

Synthetic data drawn from the model’s latent space boosts activity-classification accuracy beyond a non-augmented baseline and remains close to state-of-the-art results despite minimal task-specific tuning [82], [83]. Errors rise for activities with complex arm motion, reflecting higher limb-joint uncertainty in pose estimation. By adjusting the latent noise parameter  $\alpha$ , we generate realistic samples that preserve distributional structure and increase sample density in sparse regions, thereby mitigating the curse of dimensionality in high-dimensional feature space [84]. Even a simple convolutional network benefits from this augmentation, suggesting that richer activity models, such as those operating on continuous data streams [19], could gain further from the same framework.

## VII. LIMITATIONS

While our study demonstrates the effectiveness of probabilistic modeling and uncertainty estimation for radar-based human pose estimation, several areas merit further exploration.

Our experiments were conducted using a single sparse radar configuration with three transmitters and four receivers. While this configuration ensures computational efficiency, exploring alternative sparse radar designs could further improve pose estimation accuracy. Future work should investigate how variations in antenna placement, frequency selection, and sensor fusion strategies affect model performance, particularly in challenging motion scenarios. In addition, our dataset was collected in a controlled laboratory environment, which allows for high-fidelity evaluation but does not fully capture real-world variability. The main focus of our study was to develop a basic method for HPE from sparse radar and to reveal and interpret uncertainties. Therefore, we focused on a rather simple one-person HPE design. Future studies should investigate how our approach would perform in a multi-person estimation scenario. Testing in unconstrained environments using portable radar setups in addition to Kinect-based motion capture systems would provide insight into model robustness under different conditions, including background clutter and occlusion. Since we already developed the RadarBox system [64] for this purpose, this area will be explored in future work in more detail to test our model in real world conditions.

## VIII. CONCLUSION

Uncertainty quantification is essential for improving the interpretability and reliability of machine learning models, especially in sensor-based applications with noisy and ambiguous data. This study introduces a probabilistic approach to radar-based HPE that models uncertainties at the keypoint level, using minimally processed radar data and a latent space distribution to capture spatio-temporal dependencies.

Our RPP model achieves state-of-the-art MPJPE performance while providing meaningful uncertainty estimates, enhancing both keypoint accuracy and model transparency. The generative nature of our latent space further improves activity classification through data augmentation, addressing challenges posed by high-dimensional decision boundaries.

Beyond HPE, our findings highlight the broader potential of uncertainty-informed learning in sensor fusion, Bayesian extensions, and biomechanical modeling. By integrating uncertainty-aware methods, this work contributes to more interpretable AI systems, aligning with emerging regulatory requirements such as the EU AI Act. Future research should explore uncertainty-driven adaptation to optimize radar-based inference across diverse real-world applications.

## REFERENCES

- [1] C. Massaroni, A. Nicolò, E. Schena, and M. Sacchetti, "Remote respiratory monitoring in the time of covid-19," *Frontiers in physiology*, vol. 11, p. 635, 2020.
- [2] O. Boric-Lubecke, W. Massagram, V. M. Lubecke, A. Host-Madsen, and B. Jokanovic, "Heart rate variability assessment using doppler radar with linear demodulation," in *2008 38th European Microwave Conference*. IEEE, 2008, pp. 420–423.
- [3] M. Ogunsina, C. P. Efunniyi, O. S. Osundare, S. O. Folorunsho, and L. A. Akwawa, "Advanced sensor fusion and localization techniques for autonomous systems: A review and new approaches," *International Journal of Frontline Research in Engineering and Technology*, vol. 2, no. 1, 2024.
- [4] K. Shahriari and M. Shahriari, "Ieee standard review—ethically aligned design: A vision for prioritizing human wellbeing with artificial intelligence and autonomous systems," in *2017 IEEE Canada International Humanitarian Technology Conference (IHTC)*. IEEE, 2017, pp. 197–201.
- [5] F. Fakour, A. Mosleh, and R. Ramezani, "A structured review of literature on uncertainty in machine learning & deep learning," *arXiv preprint arXiv:2406.00332*, 2024.
- [6] E. Union, "Regulation of the european parliament and of the council laying down harmonized rules on artificial intelligence (artificial intelligence act)," 2024, official Journal of the European Union. [Online]. Available: <https://artificialintelligenceact.eu/article/13/>
- [7] S.-P. Lee, N. P. Kini, W.-H. Peng, C.-W. Ma, and J.-N. Hwang, "Hupr: A benchmark for human pose estimation using millimeter wave radar," in *Proceedings of the IEEE/CVF Winter Conference on Applications of Computer Vision*, 2023, pp. 5715–5724.
- [8] Z. Cao, J. Zhang, R. Chen, X. Guo, and G. Wang, "Task-specific feature purifying in radar-based human pose estimation," *IEEE Transactions on Aerospace and Electronic Systems*, 2023.
- [9] Z. Cao, W. Ding, R. Chen, J. Zhang, X. Guo, and G. Wang, "A joint global–local network for human pose estimation with millimeter wave radar," *IEEE Internet of Things Journal*, vol. 10, no. 1, pp. 434–446, 2022.
- [10] A. Sengupta, F. Jin, R. Zhang, and S. Cao, "mm-pose: Real-time human skeletal posture estimation using mmwave radars and cnns," *IEEE Sensors Journal*, vol. 20, no. 17, pp. 10032–10044, 2020.
- [11] Y.-H. Ho, J.-H. Cheng, S. Y. Kuan, Z. Jiang, W. Chai, H.-W. Huang, C.-L. Lin, and J.-N. Hwang, "Rt-pose: A 4d radar tensor-based 3d human pose estimation and localization benchmark," in *European Conference on Computer Vision*. Springer, 2024, pp. 107–125.
- [12] B. Zhu, Z. He, W. Xiong, G. Ding, J. Liu, T. Huang, W. Chen, and W. Xiang, "Probradarm3f: mmwave radar based human skeletal pose estimation with probability map guided multi-format feature fusion," *arXiv preprint arXiv:2405.05164*, 2024.
- [13] M. Hasan, J. Hanawa, R. Goto, R. Suzuki, H. Fukuda, Y. Kuno, and Y. Kobayashi, "Lidar-based detection, tracking, and property estimation: A contemporary review," *Neurocomputing*, vol. 506, pp. 393–405, 2022.
- [14] X. Yang, W. Shi, H. Dou, J. Qian, Y. Wang, W. Xue, S. Li, D. Ni, and P.-A. Heng, "Fetusmap: Fetal pose estimation in 3d ultrasound," in *Medical Image Computing and Computer Assisted Intervention—MICCAI 2019: 22nd International Conference, Shenzhen, China, October 13–17, 2019, Proceedings, Part V 22*. Springer, 2019, pp. 281–289.
- [15] C. Zheng, W. Wu, C. Chen, T. Yang, S. Zhu, J. Shen, N. Kehtarnavaz, and M. Shah, "Deep learning-based human pose estimation: A survey," *ACM Computing Surveys*, vol. 56, no. 1, pp. 1–37, 2023.
- [16] K. Thurn, R. Ebelt, and M. Vossiek, "Noise in homodyne fmcw radar systems and its effects on ranging precision," in *2013 IEEE MTT-S International Microwave Symposium Digest (MTT)*. IEEE, 2013, pp. 1–3.
- [17] M. A. Richards *et al.*, *Fundamentals of radar signal processing*. Mcgraw-hill New York, 2005, vol. 1.
- [18] A.-K. Seifert, M. G. Amin, and A. M. Zoubir, "Toward unobtrusive in-home gait analysis based on radar micro-doppler signatures," *IEEE Transactions on Biomedical Engineering*, vol. 66, no. 9, pp. 2629–2640, 2019.
- [19] I. Ullmann, R. G. Guendel, N. C. Kruse, F. Fioranelli, and A. Yarovoy, "A survey on radar-based continuous human activity recognition," *IEEE Journal of Microwaves*, vol. 3, no. 3, pp. 938–950, 2023.
- [20] M. I. Skolnik *et al.*, *Introduction to radar systems*. McGraw-hill New York, 1980, vol. 3.
- [21] A. Sengupta, F. Jin, and S. Cao, "Nlp based skeletal pose estimation using mmwave radar point-cloud: A simulation approach," in *2020 IEEE Radar Conference (RadarConf20)*. IEEE, 2020, pp. 1–6.
- [22] J. Müller, D. Krauß, L. Engel, M. Vossiek, B. Eskofier, and E. Dorschky, "End-to-End Learning for Human Pose Estimation from Raw Millimeter Wave Radar Data," in *Asilomar Conference on Signals, Systems, and Computers*, 2024.
- [23] S. Zhang, C. Wang, W. Dong, and B. Fan, "A survey on depth ambiguity of 3d human pose estimation," *Applied Sciences*, vol. 12, no. 20, p. 10591, 2022.
- [24] I. Sárándi, T. Linder, K. O. Arras, and B. Leibe, "How robust is 3d human pose estimation to occlusion?" in *Proceedings of the IEEE/RSJ International Conference on Intelligent Robots and Systems (IROS), Workshop on Robotic Co-Workers 4.0: Human Safety and Comfort in Human-Robot Interactive Social Environments*, 2018, workshop paper. [Online]. Available: <https://arxiv.org/abs/1808.09316>
- [25] B. Cheng, B. Xiao, J. Wang, H. Shi, T. S. Huang, and L. Zhang, "High-erhnet: Scale-aware representation learning for bottom-up human pose estimation," in *Proceedings of the IEEE/CVF conference on computer vision and pattern recognition*, 2020, pp. 5386–5395.
- [26] Z. Jiang, Z. Zhou, L. Li, W. Chai, C.-Y. Yang, and J.-N. Hwang, "Back to optimization: Diffusion-based zero-shot 3d human pose estimation," in *Proceedings of the IEEE/CVF Winter Conference on Applications of Computer Vision*, 2024, pp. 6142–6152.
- [27] Z. Zheng, J. Pan, Z. Ni, C. Shi, D. Zhang, X. Liu, and G. Fang, "Recovering human pose and shape from through-the-wall radar images," *IEEE Transactions on Geoscience and Remote Sensing*, vol. 60, pp. 1–15, 2022.
- [28] J. Fan, J. Yang, Y. Xu, and L. Xie, "Diffusion model is a good pose estimator from 3d rf-vision," in *European Conference on Computer Vision*. Springer, 2025, pp. 1–18.
- [29] H.-C. Chiang, G.-H. Li, F. Wang, S. Shirmohammadi, and C.-H. Hsu, "Enhancing skeletal pose estimation from mmwave point clouds through uncertainty reduction," in *Proceedings of the 5th International Workshop on Human-centric Multimedia Analysis*, 2024, pp. 45–53.
- [30] J. Pegoraro and M. Rossi, "Human tracking with mmwave radars: A deep learning approach with uncertainty estimation," in *2022 IEEE 23rd International Workshop on Signal Processing Advances in Wireless Communication (SPAWC)*. IEEE, 2022, pp. 1–5.
- [31] D. Feng, L. Rosenbaum, F. Timm, and K. Dietmayer, "Leveraging heteroscedastic aleatoric uncertainties for robust real-time lidar 3d object detection," in *2019 IEEE Intelligent Vehicles Symposium (IV)*. IEEE, 2019, pp. 1280–1287.
- [32] Y. Xu, Q. Huang, S. Shen, and H. Yin, "Incorporating point uncertainty in radar slam," *IEEE Robotics and Automation Letters*, 2025.

- [33] J. Zhang, Y. Chen, and Z. Tu, "Uncertainty-aware 3d human pose estimation from monocular video," in *Proceedings of the 30th ACM International Conference on Multimedia*, 2022, pp. 5102–5113.
- [34] J. N. Kundu, S. Seth, P. Y. M., V. Jampani, A. Chakraborty, and R. V. Babu, "Uncertainty-aware adaptation for self-supervised 3d human pose estimation," in *Proceedings of the IEEE/CVF conference on computer vision and pattern recognition*, 2022, pp. 20 448–20 459.
- [35] J. Gong, L. G. Foo, Z. Fan, Q. Ke, H. Rahmani, and J. Liu, "Diff-pose: Toward more reliable 3d pose estimation," in *Proceedings of the IEEE/CVF Conference on Computer Vision and Pattern Recognition*, 2023, pp. 13 041–13 051.
- [36] R. Feng, Y. Gao, T. H. E. Tse, X. Ma, and H. J. Chang, "Diffpose: Spatiotemporal diffusion model for video-based human pose estimation," in *Proceedings of the IEEE/CVF International Conference on Computer Vision*, 2023, pp. 14 861–14 872.
- [37] K. Holmquist and B. Wandt, "Diffpose: Multi-hypothesis human pose estimation using diffusion models," in *Proceedings of the IEEE/CVF international conference on computer vision*, 2023, pp. 15 977–15 987.
- [38] J. Li, S. Bian, A. Zeng, C. Wang, B. Pang, W. Liu, and C. Lu, "Human pose regression with residual log-likelihood estimation," in *Proceedings of the IEEE/CVF international conference on computer vision*, 2021, pp. 11 025–11 034.
- [39] S. K. Dwivedi, C. Schmid, H. Yi, M. J. Black, and D. Tzionas, "Poco: 3d pose and shape estimation with confidence," in *2024 International Conference on 3D Vision (3DV)*. IEEE, 2024, pp. 85–95.
- [40] S. Prokudin, P. Gehler, and S. Nowozin, "Deep directional statistics: Pose estimation with uncertainty quantification," in *Proceedings of the European conference on computer vision (ECCV)*, 2018, pp. 534–551.
- [41] L. Bramlage, M. Karg, and C. Curio, "Plausible uncertainties for human pose regression," in *Proceedings of the IEEE/CVF International Conference on Computer Vision*, 2023, pp. 15 133–15 142.
- [42] N. B. Gundavarapu, D. Srivastava, R. Mitra, A. Sharma, and A. Jain, "Structured aleatoric uncertainty in human pose estimation," in *CVPR Workshops*, vol. 2, 2019, p. 2.
- [43] A. Kendall and Y. Gal, "What uncertainties do we need in bayesian deep learning for computer vision?" *Advances in neural information processing systems*, vol. 30, 2017.
- [44] M. Stephan, T. Stadelmayer, A. Santra, G. Fischer, R. Weigel, and F. Lurz, "Radar image reconstruction from raw adc data using parametric variational autoencoder with domain adaptation," in *2020 25th International Conference on Pattern Recognition (ICPR)*. IEEE, 2021, pp. 9529–9536.
- [45] Q. Wan, J. Fang, Y. Huang, H. Duan, and H. Li, "A variational bayesian inference-inspired unrolled deep network for mimo detection," *IEEE Transactions on Signal Processing*, vol. 70, pp. 423–437, 2022.
- [46] L. Lian, A. Liu, and V. K. Lau, "User location tracking in massive mimo systems via dynamic variational bayesian inference," *IEEE Transactions on Signal Processing*, vol. 67, no. 21, pp. 5628–5642, 2019.
- [47] A. Safa, T. Verbelen, O. Catal, T. Van de Maele, M. Hartmann, B. Dhoedt, and A. Bourdoux, "Fmcw radar sensing for indoor drones using variational auto-encoders," in *2023 IEEE Radar Conference (RadarConf23)*. IEEE, 2023, pp. 1–6.
- [48] F. Jin, A. Sengupta, and S. Cao, "mmfall: Fall detection using 4-d mmwave radar and a hybrid variational rnn autoencoder," *IEEE Transactions on Automation Science and Engineering*, vol. 19, no. 2, pp. 1245–1257, 2020.
- [49] V. Kuleshov, N. Fenner, and S. Ermon, "Accurate uncertainties for deep learning using calibrated regression," in *International conference on machine learning*. PMLR, 2018, pp. 2796–2804.
- [50] D. Krauss, L. Engel, T. Ott, J. Bräunig, R. Richer, M. Gambietz, N. Albrecht, E. M. Hille, I. Ullmann, M. Braun *et al.*, "A review and tutorial on machine learning-enabled radar-based biomedical monitoring," *IEEE Open Journal of Engineering in Medicine and Biology*, 2024.
- [51] K. Ngamakeur, S. Yongchareon, J. Yu, and S. U. Rehman, "A survey on device-free indoor localization and tracking in the multi-resident environment," *ACM Computing Surveys (CSUR)*, vol. 53, no. 4, pp. 1–29, 2020.
- [52] V. C. Chen, "Micro-doppler effect of micromotion dynamics: A review," *Independent Component Analyses, Wavelets, and Neural Networks*, vol. 5102, pp. 240–249, 2003.
- [53] P. Zhao, C. X. Lu, B. Wang, N. Trigoni, and A. Markham, "Cubelearn: End-to-end learning for human motion recognition from raw mmwave radar signals," *IEEE Internet of Things Journal*, vol. 10, no. 12, pp. 10 236–10 249, 2023.
- [54] J. Giroux, M. Bouchard, and R. Laganieri, "T-fftradnet: Object detection with swin vision transformers from raw adc radar signals," in *Proceedings of the IEEE/CVF International Conference on Computer Vision*, 2023, pp. 4030–4039.
- [55] L. Chen and G. Wang, "Cpformer: End-to-end multi-person human pose estimation from raw radar cubes with transformers," *IEEE Sensors Journal*, 2025.
- [56] J. Wang, S. Tan, X. Zhen, S. Xu, F. Zheng, Z. He, and L. Shao, "Deep 3d human pose estimation: A review," *Computer Vision and Image Understanding*, vol. 210, p. 103225, 2021.
- [57] S. Choi, S. Choi, and C. Kim, "Mobilehumanpose: Toward real-time 3d human pose estimation in mobile devices," in *Proceedings of the IEEE/CVF conference on computer vision and pattern recognition*, 2021, pp. 2328–2338.
- [58] H. S. Nguyen, M. Kim, C. Im, S. Han, and J. Han, "Convnextpose: A fast accurate method for 3d human pose estimation and its ar fitness application in mobile devices," *IEEE Access*, vol. 11, pp. 117 393–117 402, 2023.
- [59] W. Zhu, X. Ma, Z. Liu, L. Liu, W. Wu, and Y. Wang, "Motionbert: A unified perspective on learning human motion representations," in *Proceedings of the IEEE/CVF international conference on computer vision*, 2023, pp. 15 085–15 099.
- [60] S. Mehraban, V. Adeli, and B. Taati, "Motionagformer: Enhancing 3d human pose estimation with a transformer-gcnformer network," in *Proceedings of the IEEE/CVF winter conference on applications of computer vision*, 2024, pp. 6920–6930.
- [61] Y. Li, S. Yang, P. Liu, S. Zhang, Y. Wang, Z. Wang, W. Yang, and S.-T. Xia, "Simcc: A simple coordinate classification perspective for human pose estimation," in *European Conference on Computer Vision*. Springer, 2022, pp. 89–106.
- [62] B. Xiao, H. Wu, and Y. Wei, "Simple baselines for human pose estimation and tracking," in *Proceedings of the European conference on computer vision (ECCV)*, 2018, pp. 466–481.
- [63] X. Sun, B. Xiao, F. Wei, S. Liang, and Y. Wei, "Integral human pose regression," in *Proceedings of the European conference on computer vision (ECCV)*, 2018, pp. 529–545.
- [64] L. Engel, J. Mueller, E. J. F. Rendon, E. Dorschky, D. Krauss, I. Ullmann, B. M. Eskofier, and M. Vossiek, "Advanced millimeter wave radar-based human pose estimation enabled by a deep learning neural network trained with optical motion capture ground truth data," *IEEE Journal of Microwaves*, pp. 1–15, 2025.
- [65] T. Instruments, "Radar system specifications," available online: (<https://www.ti.224com/tool/IWR6843AOPEVM>) [Accessed: 11, 2024].
- [66] Optitrack, "Optical motion capture system," available online: (<https://optitrack.com/cameras/flex-23913>) [Accessed: 11, 2024].
- [67] J. Wang, K. Sun, T. Cheng, B. Jiang, C. Deng, Y. Zhao, D. Liu, Y. Mu, M. Tan, X. Wang *et al.*, "Deep high-resolution representation learning for visual recognition," *IEEE transactions on pattern analysis and machine intelligence*, vol. 43, no. 10, pp. 3349–3364, 2020.
- [68] I. Habernal, "How reparametrization trick broke differentially-private text representation learning," in *Proceedings of the 60th Annual Meeting of the Association for Computational Linguistics*. Dublin, Ireland: Association for Computational Linguistics, 2022, p. (to appear). [Online]. Available: <https://arxiv.org/abs/2202.12138>
- [69] A. Amini, W. Schwarting, A. Soleimany, and D. Rus, "Deep evidential regression," *Advances in neural information processing systems*, vol. 33, pp. 14 927–14 937, 2020.
- [70] L. Dinh, J. Sohl-Dickstein, and S. Bengio, "Density estimation using real nvp," in *International Conference on Learning Representations (ICLR)*, 2017.
- [71] D. Rezende and S. Mohamed, "Variational inference with normalizing flows," in *International conference on machine learning*. PMLR, 2015, pp. 1530–1538.
- [72] S. L. Delp, F. C. Anderson, A. S. Arnold, P. Loan, A. Habib, C. T. John, E. Guendelman, and D. G. Thelen, "Opensim: open-source software to create and analyze dynamic simulations of movement," *IEEE transactions on biomedical engineering*, vol. 54, no. 11, pp. 1940–1950, 2007.
- [73] N. Meinert, J. Gawlikowski, and A. Lavin, "The unreasonable effectiveness of deep evidential regression," in *Proceedings of the AAAI Conference on Artificial Intelligence*, vol. 37, no. 8, 2023, pp. 9134–9142.
- [74] L. Berry and D. Meger, "Normalizing flow ensembles for rich aleatoric and epistemic uncertainty modeling," in *Proceedings of the AAAI Conference on Artificial Intelligence*, vol. 37, no. 6, 2023, pp. 6806–6814.
- [75] D. Gubelli, O. A. Krasnov, and O. Yarovy, "Ray-tracing simulator for radar signals propagation in radar networks," in *2013 European Radar Conference*. IEEE, 2013, pp. 73–76.

- [76] C. Schüßler, M. Hoffmann, J. Bräunig, I. Ullmann, R. Ebel, and M. Vossiek, "A realistic radar ray tracing simulator for large mimo-arrays in automotive environments," *IEEE Journal of Microwaves*, vol. 1, no. 4, pp. 962–974, 2021.
- [77] J. Tobin, R. Fong, A. Ray, J. Schneider, W. Zaremba, and P. Abbeel, "Domain randomization for transferring deep neural networks from simulation to the real world," in *2017 IEEE/RSJ international conference on intelligent robots and systems (IROS)*. IEEE, 2017, pp. 23–30.
- [78] C. A. Myers, P. J. Laz, K. B. Shelburne, and B. S. Davidson, "A probabilistic approach to quantify the impact of uncertainty propagation in musculoskeletal simulations," *Annals of biomedical engineering*, vol. 43, pp. 1098–1111, 2015.
- [79] J. M. Wakeling, M. Febrer-Nafria, and F. De Groot, "A review of the efforts to develop muscle and musculoskeletal models for biomechanics in the last 50 years," *Journal of biomechanics*, vol. 155, p. 111657, 2023.
- [80] E. Dorschky, M. Nitschke, A.-K. Seifer, A. J. van den Bogert, and B. M. Eskofier, "Estimation of gait kinematics and kinetics from inertial sensor data using optimal control of musculoskeletal models," *Journal of biomechanics*, vol. 95, p. 109278, 2019.
- [81] G. Welch, G. Bishop *et al.*, "An introduction to the kalman filter," 1995.
- [82] A. Shrestha, H. Li, J. Le Kernec, and F. Fioranelli, "Continuous human activity classification from fmcw radar with bi-lstm networks," *IEEE Sensors Journal*, vol. 20, no. 22, pp. 13 607–13 619, 2020.
- [83] M. Jia, S. Li, J. Le Kernec, S. Yang, F. Fioranelli, and O. Romain, "Human activity classification with radar signal processing and machine learning," in *2020 International conference on UK-China emerging technologies (UCET)*. IEEE, 2020, pp. 1–5.
- [84] I. Goodfellow, *Deep learning*. MIT press, 2016, vol. 196.